

# Multiscale Modeling of TiO<sub>2</sub> Nanoparticle Production in Flame Reactors: Effect of Chemical Mechanism

Maulik Mehta,<sup>†</sup> Yonduck Sung,<sup>‡</sup> Venkatramanan Raman,<sup>‡</sup> and Rodney O. Fox<sup>\*,†</sup>

*Department of Chemical and Biological Engineering, Iowa State University, Ames, Iowa 50011, and*

*Department of Aerospace Engineering and Engineering Mechanics, The University of Texas, Austin, Texas 78712*

For titanium dioxide (TiO<sub>2</sub>) nanoparticles manufactured in flame reactors, the precursor is injected into a pre-existing flame, exposing it to a high-temperature gas phase, leading to nucleation and particle growth. Predictive modeling of this chemical process requires simultaneous development of detailed chemical mechanisms describing gas-phase combustion and particle evolution, as well as advanced computational tools for describing the turbulent flow field and its interactions with the chemical processes. Here, a multiscale computational tool for flame-based TiO<sub>2</sub> nanoparticle synthesis is developed and a flamelet model representing detailed chemistry for particle nucleation is proposed. The effect of different chemical mechanisms (i.e., one-step, detailed, flamelet) on the prediction of nanoparticle nucleation is investigated using a plug-flow reactor and a partially stirred tank reactor to model the flow field. These simulations demonstrate that particle nucleation occurs much later in the flame with detailed titanium oxidation chemistry, compared to one-step chemistry. Finally, a large-eddy simulation tool is developed to study the effect of precursor injection configuration on nanoparticle formation in turbulent flames.

## Introduction

Nanoparticles have numerous applications in drug delivery, catalysis, energy, and semiconductors. Titanium dioxide (TiO<sub>2</sub>) nanoparticles are traditionally used as pigments but have found use in diverse areas such as photocatalysis<sup>1</sup> and in reducing nitrogen oxide emissions.<sup>2</sup> The production of TiO<sub>2</sub> is an important industrial process and usually occurs via a chloride process in which the titanium tetrachloride (TiCl<sub>4</sub>) precursor is oxidized in a flame reactor to produce TiO<sub>2</sub> nanoparticles.<sup>3,4</sup> Although widely used in industry, the process is not well-understood and process optimization is based mostly on experiments. Thus, gaining fundamental insight into flame reactors will lead to the manufacture of nanoparticles with more tightly controlled product properties and minimal variability. Previous modeling work has demonstrated that gas-phase reactions, which lead to particle nucleation and surface growth, and particle aggregation and sintering effects, are all important in determining the final product properties.<sup>5</sup> However, most models for TiO<sub>2</sub> production in the literature use a one-step reaction,<sup>6,7</sup> and therefore are unable to describe the role of intermediate species present in the gas-phase reactions on particle evolution.

In a flame reactor, the precursor is transported by a turbulent flow field and encounters spatially varying gas composition and temperature fields, depending on the precursor injection configuration. Both precursor transport and reaction history affect particle evolution (such as nucleation and surface growth) and determine the final properties of the nanoparticles (e.g., relative surface area). The flow structure and turbulence are very important, because they determine species and thermal energy transport and reactant mixing, flame quenching by air entrainment, and particle properties such as polydispersity, morphology, homogeneity, and crystallinity.<sup>8</sup> Thus, to predict the particle properties produced by a turbulent flame reactor, it is necessary

to have a detailed multiscale model that can capture all of the relevant processes. The gas-phase oxidation kinetics play a key role in the overall model, because they determine the rate of nanoparticle nucleation and surface growth. In turn, these kinetics are strongly coupled the combustion kinetics through the temperature-dependent rate constants (i.e., the rate of nanoparticle nucleation is enhanced at higher temperatures). The accurate modeling of flame reactors will thus require coupling of a detailed chemical mechanism for the combustion and the nanoparticle synthesis with a detailed flow solver to predict the strong coupling between the turbulent flame structure and nanoparticle formation.

In this work, the large-eddy simulation (LES) methodology is used to describe the turbulent combustion process. LES resolves all large-scale features of the flow while requiring models for small-scale processes. Although combustion occurs at the small scales, and, hence, requires modeling, LES captures the large-scale scalar mixing accurately. Several works<sup>9–14</sup> have shown that LES provides a significant increase in predictive accuracy, compared to Reynolds-averaged Navier–Stokes (RANS) calculations of the same flow configuration. For flames far from extinction, the combustion process can be modeled using the flamelet description,<sup>15</sup> where the gas-phase thermochemical composition is parametrized by a single conserved scalar. This mapping between the conserved scalar and thermochemical composition is obtained by solving the flamelet equations a priori<sup>15</sup> to the actual LES computation. Since LES is inherently three-dimensional and unsteady, the use of the flamelet approach allows very detailed chemical mechanisms to be included without significant computational cost. In the LES computation, only a transport equation for the conserved scalar is evolved.

When nanoparticle synthesis is considered, the gas-phase thermochemical composition also consists of the species pertaining to the precursor evolution. Since the precursor chemistry contains irreversible reactions, the validity of the flamelet assumption under such conditions must be evaluated. In this study, we are particularly interested in the effect of the chemical mechanism (i.e., one-step, detailed, and flamelet) on the

\* To whom correspondence should be addressed. Tel.: +1 (515) 294-9104. Fax: +1 (515) 294-2689. E-mail: rofox@iastate.edu.

<sup>†</sup> Iowa State University.

<sup>‡</sup> The University of Texas at Austin.

nucleation rate of nanoparticles, and the location of the maximum nucleation rate, with respect to the flame surface. Therefore, our primary objective is to determine whether the one-step reaction provides an adequate approximation of the detailed chemistry proposed by West et al.<sup>5</sup> To accomplish this objective, we develop a sequence of canonical test problems that are simulated directly, using the detailed chemistry mechanism or through the flamelet assumption. We first model the flame reactor as a plug-flow reactor (PFR) to examine the time evolution of the number density of nuclei and its coupling with the flame chemistry. Then, to account for realistic flow conditions and mixing effects, we use a partially stirred tank reactor (PaSR) as a model for a nonpremixed flame reactor. Finally, to capture the detailed structure of the turbulent flame, a LES of turbulent combustion is used to model a flame reactor. All the flow models are set up according to conditions used in experimental studies (see Figure 1, presented later in this paper).<sup>16</sup> For each reactor model, a population balance equation (PBE) for particle nucleation and aggregation is coupled to the chemistry mechanism and solved using the quadrature method of moments (QMOM).<sup>17</sup>

### Multiscale Model Description

**Chemical Kinetic Models.** Although widely used in industry, the chloride process is not well-understood and the kinetics for this process remain incomplete.<sup>18</sup> Previous studies<sup>18,19</sup> based on experiments have been performed to investigate the chemical mechanism for the chloride process. Pratsinis et al.<sup>19</sup> investigated the oxidation of TiCl<sub>4</sub> vapor between 700–1000 °C and reported the overall oxidation kinetics of TiCl<sub>4</sub> as a one-step reaction. The rate is first order, with respect to TiCl<sub>4</sub>, and nearly zero order for O<sub>2</sub> up to a 10-fold oxygen excess. This rate has been the basis of many numerical studies of TiO<sub>2</sub> nanoparticle formation.<sup>6,7,20–23</sup> However, the experiments used to develop the kinetic expression were performed at much lower temperatures than those encountered in flame reactors; hence, the use of one-step kinetics at higher temperatures should be done with caution.

Generally, the chemical kinetics of TiCl<sub>4</sub> oxidation can be represented by chemical mechanisms with different degrees of complexity. For example, Spicer et al.<sup>7</sup> used an overall oxidation rate constant with the surface growth expression of Ghosh-tagore<sup>24</sup> to propose a nucleation expression based on a one-step reaction:



The rate expression is given by

$$\frac{d[\text{TiCl}_4]}{dt} = -k_{\text{total}}(T)[\text{TiCl}_4] \quad (2)$$

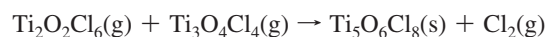
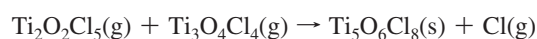
where the overall oxidation rate constant is

$$k_{\text{total}}(T) (\text{s}^{-1}) = 8.26 \times 10^4 \exp\left(-\frac{10681}{T}\right) \quad (3)$$

Here,  $T$  is the gas-phase temperature (given in Kelvin) and  $[\text{TiCl}_4]$  is the concentration of TiCl<sub>4</sub>. The one-step reaction does not account for the role of intermediate species encountered in flame reactors on nanoparticle formation events. As noted above, the oxidation and surface growth rates in the one-step reaction are based on experiments that were performed at much lower temperatures than those encountered in flame reactors.

It has been argued<sup>25</sup> that the accurate modeling of nanoparticle formation in a flame reactor requires a detailed chemical mechanism that can properly represent the complex chemistry encountered in flames. In the past, the absence of thermochemical data prevented any simulations using detailed chemistry. West et al.<sup>26</sup> performed density functional theory (DFT)-based quantum calculations to determine the necessary thermochemical data and proposed the first thermodynamically consistent mechanism for TiCl<sub>4</sub> oxidation containing 25 species and 51 reactions,<sup>5</sup> and recently extended it to 30 species and 66 reactions.<sup>25</sup> Thermodynamic equilibrium studies based on the mechanism of West et al.<sup>26</sup> suggest that, at temperatures of >600 K, the critical nucleus size contains at least five Ti atoms. However, this mechanism does not include any species involving more than three Ti atoms; therefore, it must be augmented with additional reactions before it can be used to predict nanoparticle nucleation.

Following the suggestion of West et al.,<sup>5</sup> in this work, we add three collision-limited reactions to the mechanism of West et al.,<sup>25</sup> to represent nanoparticle nucleation:



The resulting detailed mechanism, along with GRI-Mech 2.11 for methane combustion,<sup>27</sup> containing a total of 76 species and 348 reactions, is referenced hereafter as the detailed kinetic mechanism.

**Flamelet Tables.** The flamelet model parametrizes the thermochemical composition of the gas phase using the mixture fraction, which is a conserved scalar.<sup>15</sup> The steady-flamelet assumption has been used successfully to model a wide-range of flame configurations.<sup>9,10,12,15,28</sup> In the steady-flamelet model, one-dimensional flamelet equations are solved a priori and the results stored in a lookup table. Essentially, the one-dimensional equations correspond to a counter-diffusion flame.<sup>15</sup> Any gas-phase composition,  $\phi$ , can be retrieved as

$$\phi = \mathcal{K}(\xi, \chi) \quad (4)$$

where  $\mathcal{K}$  is the flamelet mapping,  $\xi$  the mixture fraction, and  $\chi$  the stoichiometric mixture fraction dissipation rate. Here, the scalar dissipation rate is fixed at 15.566 s<sup>-1</sup> for the LES simulation, which corresponds to a strained flame that is still far from extinction. In both the PaSR and LES simulations described below, the mixture fraction is evolved as a scalar and the gas-phase composition obtained using the above relation. The flamelet tables are constructed using the FlameMaster code.<sup>29</sup> The mixture–fraction dimension in the lookup table is discretized using 1000 points. Note that using a single mixture fraction restricts the applicability of the flamelet table to reactor with two inlet streams.<sup>30</sup>

**Population Balance Model.** After nucleation, nanoparticles in a flame will aggregate due to Brownian collisions and can undergo changes in shape (i.e., sintering). The evolution of the size distribution of nanoparticles in a flame reactor can be represented using a nonlinear integral-differential equation called the population balance equation (PBE), which describes the evolution of the particle size distribution (PSD). When describing the PSD evolution due to nucleation, surface growth and aggregation, the PBE can be represented by a single variable (e.g., particle volume). However, the presence of sintering requires the introduction of an additional variable: surface area.

The use of CFD techniques to model a turbulent flame requires the solution of the PBE at every grid point. Thus, the accurate solution of the PBE, when being computationally viable, is essential in the multiscale modeling of flame reactors.

TiO<sub>2</sub> synthesis with simultaneous nucleation, surface growth, aggregation, and sintering has been modeled using sectional methods,<sup>31</sup> moving sectional population balance models,<sup>7</sup> and stochastic techniques.<sup>5</sup> The sectional methods, although they solve for the full PSD, suffer from the problem of numerical diffusion. Decreasing the sectional spacing could minimize numerical diffusion; however, this results in a significant increase in computation time.<sup>7</sup> Thus, accurate sectional methods are computationally intractable for CFD applications. Stochastic methods can also solve for the full PSD but, to reduce the statistical error occurring in such simulations, the number of particles required must be extremely large, which would lead to increased computation time.<sup>32</sup> As a consequence, incorporation of stochastic methods into CFD applications is also not computationally tractable.

An alternative to these approaches is the method of moments (MOM). A particular class of moment methods called the quadrature method of moments (QMOM) has found popularity when the PBE can be represented by only one internal coordinate.<sup>32,33</sup> QMOM can be thought of as a presumed PSD method with the PSD represented by weighted delta functions. The closure problem that arises by this representation is solved by determining the weights and abscissas using the quadrature approximation.<sup>34</sup> These methods are especially useful for CFD applications, because they require the solution of a relatively small number of scalars (moments) at each grid point. Thus, QMOM provides us with an attractive alternative to solve the PBE while being computationally viable. Recently, Cheng et al.<sup>35</sup> introduced a conditional QMOM (CQMOM) that can be used to solve PBEs represented by two internal coordinates, making the QMOM applicable for the cases where sintering is also considered in the PBE.

The evolution of nanoparticles in a turbulent flame reactor can be described by a volume-surface PBE containing terms for (1) nucleation, (2) surface growth, (3) aggregation, and (4) sintering.<sup>31</sup> In the nucleation step, nuclei with a given volume and surface area are formed from the gas-phase species, as described above. For surface growth, the gas-phase species oxidize directly on the nanoparticle surface, instead of forming nuclei. The aggregation step proceeds through particle-particle collisions, the frequencies of which depend on the nanoparticle volumes and gas-phase properties (e.g., temperature and viscosity). The sintering step is modeled as a temperature-dependent surface-relaxation process, wherein a particle with a given volume tends toward a spherical shape. Note that because sintering occurs after particle nucleation and aggregation, and it is much faster at high temperatures (such as inside the flame), the relative amount of sintering will depend strongly on whether the particles are formed before or after the flame surface.

Nanoparticle nucleation is an important first step that leads to further particle evolution events. Since this work aims to look at the effect of the chemical mechanism on nucleation events, we only account for the nucleation and aggregation events in our PBE. The corresponding univariate PBE is given by

$$\frac{\partial n(v)}{\partial t} + \frac{\partial U_i n(v)}{\partial x_i} = S(T, \phi) \delta(v - v_0) + \frac{1}{2} \int_0^v n(v-u) n(u) q(v-u, u) du - n(v) \int_0^\infty n(u) q(v, u) du \quad (5)$$

where  $n(v)$  (expressed in units of m<sup>-3</sup>) is the number density function (NDF) of nanoparticles with volume  $v$ ,  $\phi$  denotes the gas-phase species molar concentrations,  $v_0$  is the volume of a nuclei,  $q(v, u)$  is the aggregation kernel,  $U_i$  is the gas-phase fluid velocity and repeated Roman indices imply summation. For the one-step reaction, the nucleation rate is given by

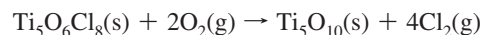
$$S(T, \phi) = \max(0, k_{\text{total}} - k_s A) N_{\text{av}} [\text{TiCl}_4] \quad (6)$$

where  $N_{\text{av}}$  is Avogadro's number, the surface reaction rate constant is

$$k_s(T) \text{ (m/s)} = 49 \exp\left(-\frac{8993}{T}\right) \quad (7)$$

and  $A$  is the particle surface area concentration (given in units of m<sup>2</sup>/m<sup>3</sup>;  $A = \pi m_0 [6m_1 / (\pi m_0)]^{2/3}$ , where  $m_0$  and  $m_1$  are moments of the PSD discussed below). Note that for the one-step reaction, each TiO<sub>2</sub> molecule is treated as a nuclei with  $v_0 = 3.32 \times 10^{-29}$  m<sup>3</sup>, and, thus (in the absence of aggregation, where  $m_1/m_0 = v_0$ ), the one-step reaction will produce a larger number of nanoparticles.

To take into account the effect of the intermediate species encountered in a flame reactor on the nucleation event, for the detailed mechanism, the postulated reaction leading to the formation of Ti<sub>5</sub>O<sub>6</sub>Cl<sub>8</sub> is treated as a nucleation event with each Ti<sub>5</sub>O<sub>6</sub>Cl<sub>8</sub> molecule treated as a nuclei. Note that the Ti<sub>5</sub>O<sub>6</sub>Cl<sub>8</sub> is assumed to undergo an instantaneous surface oxidation reaction to replace the Cl atoms by O atoms:



so that the final composition of the nuclei is Ti<sub>5</sub>O<sub>10</sub> with  $v_0 = 16.60 \times 10^{-29}$  m<sup>3</sup>. Thus, in comparison to the one-step reaction, the detailed mechanism will produce five times less nuclei for the same amount of TiCl<sub>4</sub> oxidized. These assumptions result in a nucleation rate defined as

$$S(T, \phi) = k_{\text{nuc}} N_{\text{av}} [\text{Ti}_5\text{O}_6\text{Cl}_8] [\text{O}_2]^2 \quad (8)$$

where the gas-phase chemical concentrations appearing on the right-hand side are found from the detailed kinetic model. This reaction is assumed to be diffusion-limited and irreversible, so that the pre-exponential factor is  $k_{\text{nuc}} = 10^{25}$  cm<sup>6</sup>/(mol<sup>2</sup> s) and the activation energy in the exothermic direction is zero.

As nanoparticles nucleate, they can collide with each other, leading to the formation of clusters of nuclei. These clusters may also collide with each other in a manner that leads to even bigger aggregates. The rate of aggregation depends on the collision frequency. Assuming the particle collisions are generated by Brownian motion, the collision kernel for aggregation of a particle of size  $v$  with another particle of size  $u$  is given by<sup>36</sup>

$$q(v, u) = \frac{2RT}{3\mu N_{\text{av}}} \left( \frac{1}{v^{1/d_f}} + \frac{1}{u^{1/d_f}} \right) (v^{1/d_f} + u^{1/d_f}) \quad (9)$$

where  $R$  is the gas constant,  $\mu$  the gas viscosity, and  $d_f$  is the fractal dimension (which is taken to be 2.5, assuming diffusion-limited aggregation). Note that (1) the aggregation rate is proportional to the gas-phase temperature, and, therefore, (2) aggregation will be faster near the flame surface.

The direct solution of the PBE in a turbulent flow solver is intractable and unnecessary. Instead, using a MOM, the volume moments are defined by

$$m_k = \int_0^\infty v^k n(v) dv \quad (10)$$

These moments have physical significance and can be compared to experimental data. For example, the zero-order moment  $m_0$  is the particle number density (or particle concentration), and  $m_1$  is the particle volume density (which is directly proportional to the mass concentration since the density of the solid is constant). Comparison of the lower-order moments between different chemical mechanisms will give us an idea about the effect of the chemical mechanism on nucleation.

The PBE in eq 5 can then be replaced by the transport equations for the volume moments:

$$\frac{\partial m_k}{\partial t} + \frac{\partial U_i m_k}{\partial x_i} = S(T, \phi) v_0^k + \int_0^\infty v^k \left( \frac{1}{2} \int_0^v n(v-u) n(u) q(v-u, u) du - n(v) \int_0^\infty n(u) q(v, u) du \right) dv \quad (11)$$

where the aggregation term is not closed. In this work, the aggregation term is closed using QMOM.<sup>17,34</sup> In the three flow models (PFR, PaSR, LES) for the flame reactor, the PBE is represented by six moment transport equations based on volume (eq 11 with  $k = 0, 1, \dots, 5$ ), all tightly coupled to the chemical kinetic model and the gas-phase temperature through  $S(T, \phi)$  and  $q(v, u)$ .

**PFR Model.** The flame reactor is first modeled as a partially premixed jet of precursor/fuel/air entraining the surrounding air. The plug-flow assumption allows us to compare the evolution of the volume moments of the NDF for each chemical mechanism under idealized conditions (i.e., no back mixing of fluid). Initial conditions for the PFR are found from the mass flow rates of CH<sub>4</sub> (fuel), TiCl<sub>4</sub> (precursor), argon (inert gas), and air (oxidant) for Flame 11 in Pratsinis et al.<sup>16</sup> Since the temperature and concentrations in a PFR evolve with time, because of chemical reactions and the entrainment of air, the flamelet assumption is not directly applicable.<sup>30</sup> Therefore, only the one-step method and the detailed mechanisms are compared in the PFR.

The partially premixed PFR is modeled assuming a two-environment micromixing model,<sup>30</sup> where a round jet of precursor/fuel/air issuing from the central nozzle (Environment 1) entrains the surrounding air (Environment 2). The evolution of composition variables in Environment 1 ( $\langle \phi \rangle_1$ ) can be represented by

$$\frac{dp_1}{d\tau} = \gamma(1 - p_1)p_1 \quad (12a)$$

$$\frac{d\langle \phi \rangle_1}{d\tau} = \gamma(1 - p_1)(\langle \phi \rangle_2 - \langle \phi \rangle_1) + \frac{d_{\text{jet}}}{v_{\text{jet}}} S(\langle \phi \rangle_1) \quad (12b)$$

where  $\tau$  is the dimensionless time from which the fluid left the nozzle ( $\tau = tv_{\text{jet}}/d_{\text{jet}}$ ),  $v_{\text{jet}}$  the inlet velocity of the jet,  $d_{\text{jet}}$  the mass fraction of Environment 1,  $\langle \phi \rangle_i$  the composition vector of the  $i$ th environment,  $\gamma = 0.0094$  is the spreading rate of a turbulent round jet,<sup>37</sup> and  $S$  represents the composition source term due to chemical reactions. We assume that no reactions occur in Environment 2, and, thus,  $\langle \phi \rangle_2$  is constant (i.e., found from the conditions of the surrounding air). The initial condition for  $p_1$  is set to  $p = 1.415 \times 10^{-5}$ , and that for  $\langle \phi \rangle_1$  is discussed below. Note that  $p_1$  grows monotonously toward unity, representing the entrainment of surrounding air.

**PaSR Model.** To relax the highly idealized mixing assumptions used in the PFR, a PaSR is also used to model the flame reactor under partially stirred conditions. PaSR models, which

are essentially the application of a stochastic Monte Carlo process to approximate the solution of the transport equation for the joint probability density function (PDF) of all reactive species,<sup>38</sup> can be used to model well-macromixed turbulent reacting flows. In the modeling of turbulent reacting flows based on PDF methods, the fluid composition changes by both reaction source terms and mixing.<sup>30</sup> The change in composition due to reaction is treated exactly, while molecular mixing must be modeled. Modeling mixing in a PaSR involves prescribing the evolution of stochastic particles in such a way that they mimic the change in composition of a fluid particle due to mixing in a turbulent reactive flow.<sup>39</sup> In the PaSR, the residence time distribution is assumed to be exponential, corresponding to a well-macromixed reactor.<sup>30</sup> Thus, in comparison to the PFR with no back mixing between fluid particles, the PaSR has maximum back mixing of the fluid.

In this work, the stochastic simulation of the PaSR uses 1000 particles ( $n$ ). Each particle carries information about its mixture fraction, enthalpy, species mass fractions ( $\phi$ ), and six volume moments. The PaSR is fed with two inlet streams: one stream injecting TiCl<sub>4</sub>, mixed with CH<sub>4</sub> and argon, and the other stream injecting air with mass flow rates corresponding to Flame 11 from Pratsinis et al.<sup>16</sup> The mean residence time for each particle in the PaSR is  $15.4 \times 10^{-2}$  s. The modified Curl's approach<sup>39</sup> is used to model molecular mixing in the PaSR with a characteristic mixing time of  $1.25 \times 10^{-2}$  s. The initial conditions are set to ensure that combustion occurs, and the simulation is allowed to reach steady state (approximated three mean residence times) before data are collected.

**LES Model.** To demonstrate the applicability of the flamelet-based combustion models for nanoparticle synthesis, a verification study based on an experimental flame will be conducted here. The experiment will be simulated using the large-eddy simulation (LES) methodology. LES has been demonstrated to be a highly predictive tool for chemically reactive turbulent flows.<sup>9,11,30</sup> In LES, the flow field is decomposed into resolved and subfilter fields, and only the resolved field is directly computed on an Eulerian grid. The filtering operation of a scalar  $Q$  in variable-density flows can be represented as

$$\bar{Q}(\mathbf{y}, t) = \frac{1}{\bar{\rho}} \int \rho Q(\mathbf{x}, t) G(\mathbf{x} - \mathbf{y}) d\mathbf{x} \quad (13)$$

where  $G$  is the filtering kernel,  $\bar{\rho}$  the filtered density, and  $\rho$  the unfiltered density. The filtering operation is applied to the continuity and momentum equations to obtain the following LES flow equations:

$$\frac{\partial \bar{\rho}}{\partial t} + \frac{\partial \bar{\rho} \bar{u}_i}{\partial x_i} = 0 \quad (14)$$

$$\frac{\partial \bar{\rho} \bar{u}_i}{\partial t} + \frac{\partial \bar{\rho} \bar{u}_i \bar{u}_j}{\partial x_j} = -\frac{\partial \bar{P}}{\partial x_i} + \frac{\partial \tau_{ij}}{\partial x_j} - \frac{\partial T_{ij}}{\partial x_j} \quad (15)$$

where  $\tau_{ij}$  is the viscous stress tensor, given by

$$\tau_{ij} = \mu \left( \frac{\partial \bar{u}_i}{\partial x_j} + \frac{\partial \bar{u}_j}{\partial x_i} \right) \quad (16)$$

and  $T_{ij}$  denotes the subfilter stresses ( $T_{ij} = \bar{\rho} \bar{u}_i \bar{u}_j - \bar{\rho} \bar{u}_i \bar{u}_j$ ).

The flamelet chemistry requires a conserved scalar to be evolved, along with the flow equations. The transport equation for the conserved scalar can be written as

$$\frac{\partial \bar{\rho} \tilde{Z}}{\partial t} + \frac{\partial \bar{\rho} \tilde{u}_j \tilde{Z}}{\partial x_j} = \overline{\frac{\partial}{\partial x_j} \left( \rho D \frac{\partial Z}{\partial x_j} \right)} - \frac{\partial \mathbf{M}_Z}{\partial x_j} \quad (17)$$

where  $\mathbf{M}_Z = \bar{\rho} \tilde{u}_j \tilde{Z} - \overline{\bar{\rho} \tilde{u}_j \tilde{Z}}$ . The diffusion term can be approximated by

$$\overline{\frac{\partial}{\partial x_j} \left( \rho D \frac{\partial Z}{\partial x_j} \right)} = \frac{\partial}{\partial x_j} \left( \bar{\rho} \tilde{D} \frac{\partial \tilde{Z}}{\partial x_j} \right) \quad (18)$$

where  $\tilde{D}$  is obtained from the flamelet look-up table. For the sake of simplicity,  $\tilde{D}$  is written as  $D$  henceforth.

Both  $T_{ij}$  and  $\mathbf{M}_Z$  require closure models. The subfilter stress is modeled using the gradient diffusion hypothesis:<sup>40,41</sup>

$$\bar{\rho} \left( T_{ij} - \frac{\delta_{ij}}{3} T_{kk} \right) = -2 \bar{\rho} \nu_t \left( S_{ij} - \frac{\delta_{ij}}{3} \tilde{u}_{kk} \right) \quad (19)$$

where  $S_{ij}$  is the rate-of-strain tensor. The eddy viscosity  $\nu_t$  is obtained using the Smagorinsky model<sup>40</sup> as

$$\nu_t = C_s \Delta^2 \mathcal{S} \quad (20)$$

where  $\mathcal{S}$  is the magnitude of the strain rate and  $\Delta$  is the characteristic width of the filter. The coefficient  $C_s$  is determined using a dynamic procedure.<sup>42,43</sup> The subfilter scalar flux is also modeled using a gradient-diffusion hypothesis as

$$\mathbf{M}_Z = -\bar{\rho} D_t \frac{\partial \tilde{Z}}{\partial x_j} \quad (21)$$

where  $D_t$  is the eddy diffusivity. The eddy diffusivity is computed using a formulation similar to the eddy viscosity:

$$D_t = C_z \Delta^2 \mathcal{S} \quad (22)$$

where  $C_z$  is determined dynamically.<sup>42</sup> The filtered gas-phase composition is obtained by assuming that the subfilter distribution of mixture fraction is a  $\beta$ -function,<sup>44</sup> which is parametrized using the filtered mixture fraction and its variance. The mixture-fraction variance is obtained using the dynamic model of Pierce and Moin.<sup>45</sup>

For the purpose of this study, only the one-step precursor chemistry is simulated. A separate transport equation for the precursor concentration is evolved. This transport equation is identical to the conserved scalar equation but contains a chemical source term on the right-hand side. This source term is  $S(T, \phi)$  in eq 6 multiplied by the fluid density. The nanoparticle population is obtained by solving the filtered form of eq 11. The LES filtered equations are solved using a second-order energy-conserving low-Mach number scheme.<sup>46–48</sup> A third-order upwind scheme is used to evolve the scalar transport equations.<sup>49,50</sup>

Consistent with binary mixing description used in the flamelet model, the configuration studied in this work is based on the Flame D.<sup>16</sup> The flow configuration consists of three coaxial injectors with fuel and precursor issuing from the innermost port while air issues through the outer port. The second port is inactive in this experiment. Details of the burner geometry can be found in Pratsinis et al.<sup>16</sup> The burner geometry consists of the central nozzle with diameter  $D = 4$  mm and the two annuli with the space of 0.5 mm. The innermost and outermost walls have the thickness of 1 mm while the middle wall has a thickness of 0.5 mm. The flow rates of the gases are given as  $5.8 \times 10^4$  mol/min for the precursor ( $\text{TiCl}_4$ ), 0.312 L/min for the fuel ( $\text{CH}_4$ ), and 0.250 L/min for the diluent gas (argon),

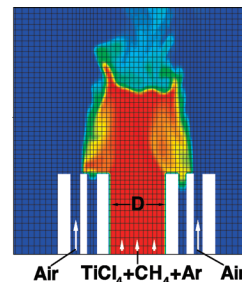


**Figure 1.** Configuration of inlets for flame reactor corresponding to the experiment; a LES computational mesh with one out of four grid cells is overlaid on the mixture–fraction contours.

**Table 1. Initial Conditions for PFR**

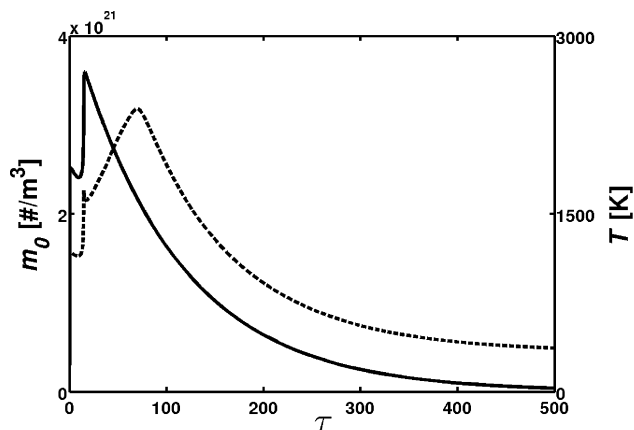
parameter	Environment 1	Environment 2
temperature	1080 K	333 K
Ar content (mass fraction)	0.332	0
$\text{CH}_4$ content (mass fraction)	0.166	0
$\text{N}_2$ content (mass fraction)	0.309	0.767
$\text{O}_2$ content (mass fraction)	0.094	0.233
$\text{TiCl}_4$ content (mass fraction)	0.099	0

respectively. An air stream of 5.5 L/min is provided from the outermost injector. The inlet configuration used in the LES model is shown in Figure 1. The simulation domain used to model the turbulent flame is  $40D$  long with a radius of  $10D$ . A  $256 \times 96 \times 32$  computational grid is used in the cylindrical coordinate reference frame. As seen from Figure 1, the grid cells are heavily clustered near the reactor exit, where the turbulent mixing is most intensive. A laminar velocity profile is used for the inlet for the central jet due to its low Reynolds number. The code is run on 128 processors, using an MPI-based domain decomposition strategy.

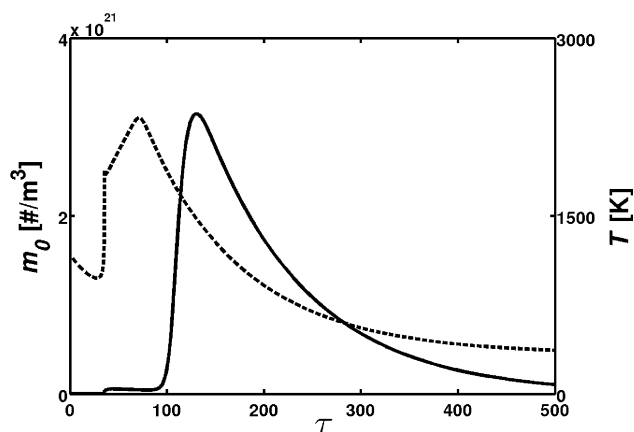
## Results and Discussion

**PFR Results.** The PFR model is used for both the one-step and the detailed nucleation mechanisms with the initial conditions given in Table 1. For the PFR results, only nucleation is considered and particle aggregation is disabled in the models. The temperature profiles for both cases evolve similarly (see Figure 2). The maximum flame temperature occurs at  $\tau \approx 80$ , but the evolution of number density ( $m_0$ ) follows a different pattern for each case. For the one-step mechanism (see Figure 2a),  $\text{TiCl}_4$  is consumed very rapidly at temperatures of  $>1000$  K, so that all of the nucleation occurs by  $\tau = 15$ , after which the number density decreases as the jet is diluted with air. In comparison, the detailed nucleation model (see Figure 2b) produces a relatively small number particles at  $\tau \approx 30$ , followed by a much larger number after  $\tau = 100$  (i.e., after the flame surface).

With the detailed nucleation mechanism, the maximum nucleation rate occurs in the temperature range  $T = 1500$ – $1800$  K, while outside this range nucleation is negligible. Because, in the PFR, the flame temperature passes through this range on both the rich side ( $\tau < 90$ ) and the lean side ( $\tau > 90$ ) of the flame, two bursts of nucleation are observed. In contrast, for the one-step nucleation mechanism, the precursor is completely reacted once the temperature reaches 1600 K for the first time ( $\tau < 30$ ). These observations imply that, for the one-step reaction, all of the particles will be formed upstream of the flame surface, and then will subsequently pass through the high-temperature region of the flame, where particle sintering can occur. In contrast, for the detailed mechanism, most of the particles are formed downstream from the high-temperature flame surface



(a) One-step nucleation



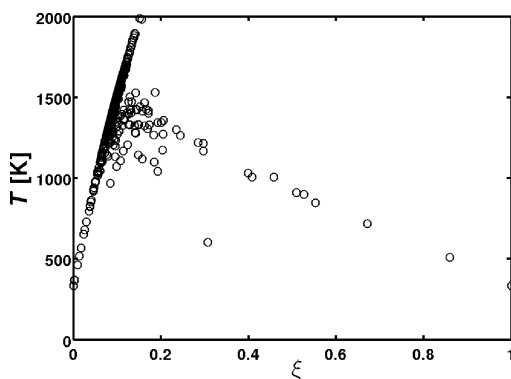
(b) Detailed nucleation

Figure 2. Evolution of number density (solid) and temperature (dashed) in PaSR.

Table 2. Inlet Conditions for PaSR and LES

parameter	initial	stream 1	stream 2
mass flow rate		97.08 mg/s	10.92 mg/s
temperature	1400 K	333 K	333 K
Ar content (mass fraction)	0	0	0.555
CH <sub>4</sub> content (mass fraction)	0	0	0.278
N <sub>2</sub> content (mass fraction)	0.767	0.767	0
O <sub>2</sub> content (mass fraction)	0.233	0.233	0
TiCl <sub>4</sub> content (mass fraction)	0	0	0.167

and, hence, would be less susceptible to sintering. Thus, we can conclude that the choice of the nucleation model will have



(a) Detailed flame chemistry

Table 3. Average Temperature, Number Density, and Cluster Diameter in PaSR

case	average temperature, $\langle T \rangle$ (K)	average number density, $\langle m_0 \rangle$ (m <sup>-3</sup> )	average cluster diameter, $\langle d_p \rangle$ (nm)
detailed flame chemistry, one-step nucleation	1440	$7.26 \times 10^{18}$	6.92
detailed flame chemistry, detailed nucleation	1408	$1.06 \times 10^{18}$	5.48
flamelet, one-step nucleation	1305	$1.76 \times 10^{19}$	8.38
flamelet, detailed nucleation	1328	$4.54 \times 10^{17}$	3.47
all flamelet with one-step nucleation	1303	$1.78 \times 10^{19}$	8.46
all flamelet with detailed nucleation	1316	$2.04 \times 10^{18}$	5.86

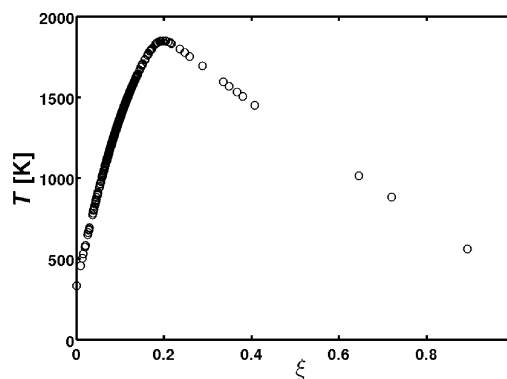
a strong effect on the predicted particle properties (e.g., sintered versus nonsintered), since the two models predict very different locations in the flame for particle nucleation.

**PaSR Results.** The PaSR model with the inlet conditions given in Table 2 is used to run the six different cases listed in Table 3. The combustion chemistry is treated using either the detailed kinetic mechanism or a flamelet approximation. The nucleation chemistry is treated using either one-step or detailed chemistry. In the two “all flamelet” cases, the combustion and nucleation chemistry are tabulated into one flamelet table.

Neglecting surface growth, we find that each particle cluster contains a collection of primary particles. The total number of primary particles  $N_p$  in an agglomerate is related to the particle diameter  $d_p$  through a power-law expression based on the fractal dimension<sup>36</sup>

$$N_p = A \left( \frac{d_p}{d_{po}} \right)^{d_f} \quad (23)$$

where  $d_{po}$  is the diameter of monodispersed primary particle, found from the respective  $v_0$  value. For one-step operation,  $d_{po} = 3.98 \times 10^{-10}$  m and for the detailed nucleation,  $d_{po} = 6.82 \times 10^{-10}$  m. The value of  $A$  varies with different values of  $d_f$ ; however, if eq 23 holds for  $d_p \rightarrow d_{po}$  ( $N_p \rightarrow 1$ ), then  $A$  has a value of unity. The total volume of the cluster can then be calculated by multiplying  $N_p$  by the primary particle volume  $v_0$ . The total volume of the cluster can also be found by dividing the first volume moment ( $m_1$ ) by the zeroth volume moment ( $m_0$ ). This leads to



(b) Flamelet chemistry

Figure 3. Scatter plots of temperature ( $T$ ) versus mixture fraction ( $\xi$ ) in PaSR.

$$N_p v_0 = \left( \frac{m_1}{m_0} \right) \quad (24)$$

Using the expression from eq 23 for  $N_p$ , we then can find the particle diameter  $d_p$ :

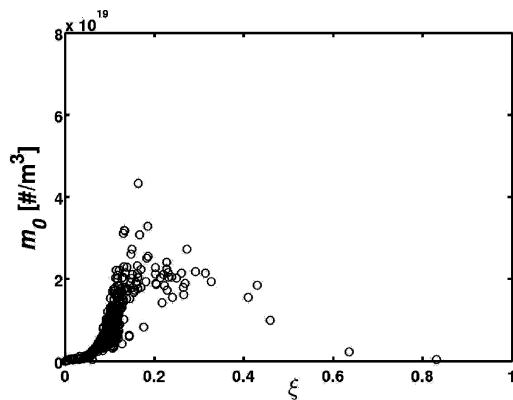
$$d_p = d_{po} \left( \frac{m_1}{m_0 v_0} \right)^{1/d_t} \quad (25)$$

The results reported in Table 3 were averaged over all  $n$  particles used in the PaSR. Thus, the following equations give us the average value of  $T$ ,  $m_0$ , and  $d_p$ , respectively:

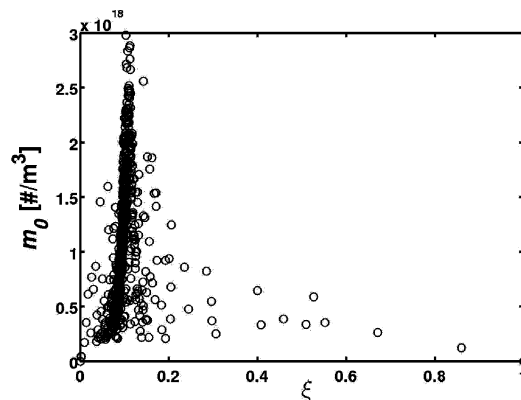
$$\langle T \rangle = \frac{\sum_{i=0}^n T(i)}{n} \quad (26a)$$

$$\langle m_0 \rangle = \frac{\sum_{i=0}^n m_0(i)}{n} \quad (26b)$$

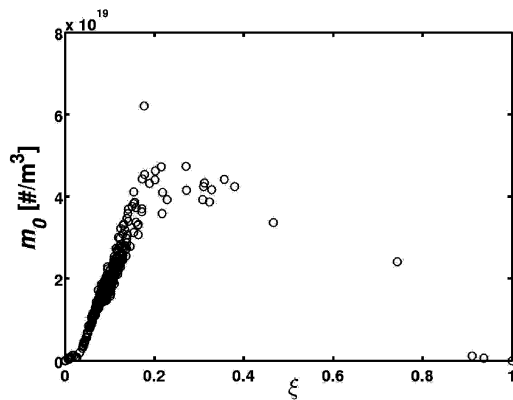
$$\langle d_p \rangle = \frac{\sum_{i=0}^n d_p(i)}{n} \quad (26c)$$



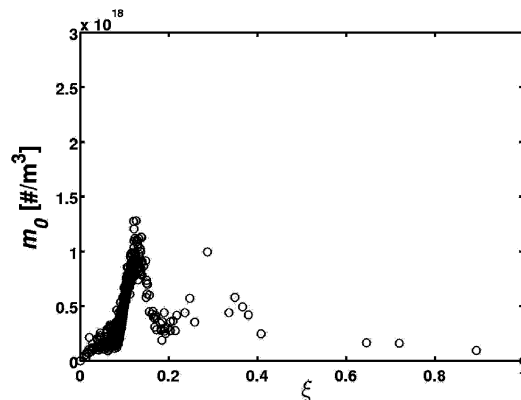
(a) Detailed flame, one-step nucleation



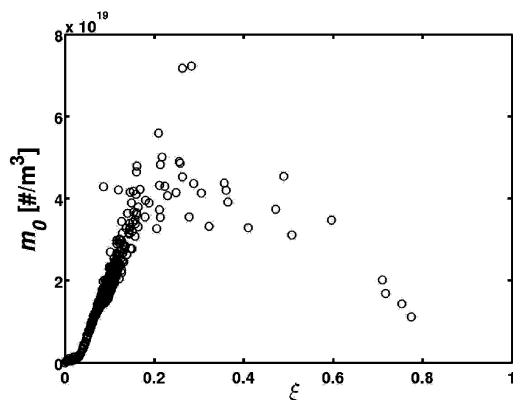
(b) Detailed flame, detailed nucleation



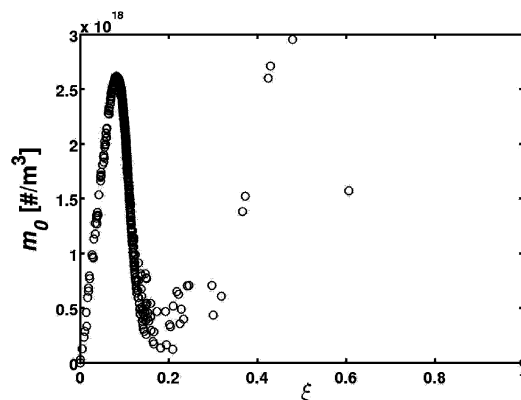
(c) Flamelet, one-step nucleation



(d) Flamelet, detailed nucleation

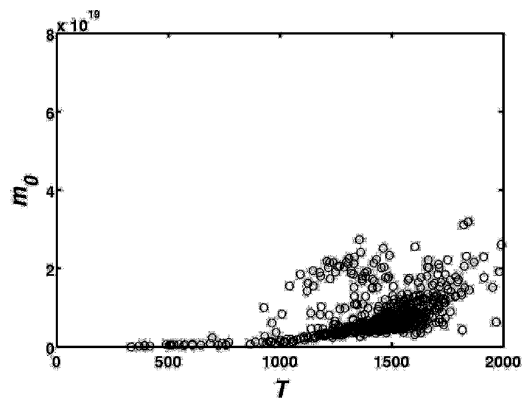


(e) All flamelet, one-step nucleation

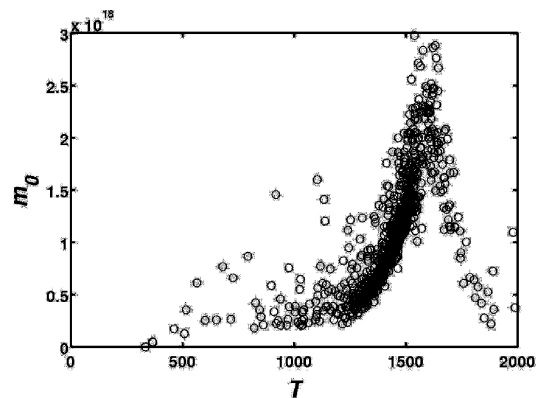


(f) All flamelet, detailed nucleation

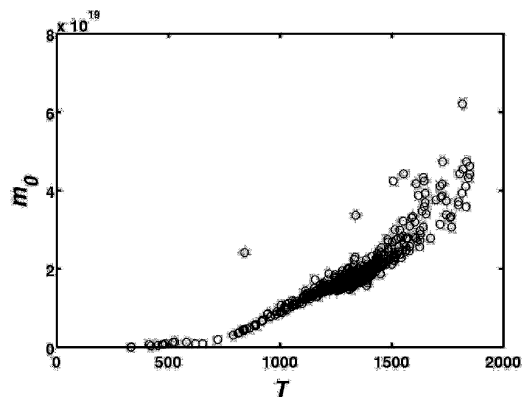
Figure 4. Scatter plots of number density ( $m_0$ ) versus mixture fraction ( $\xi$ ) in PaSR.



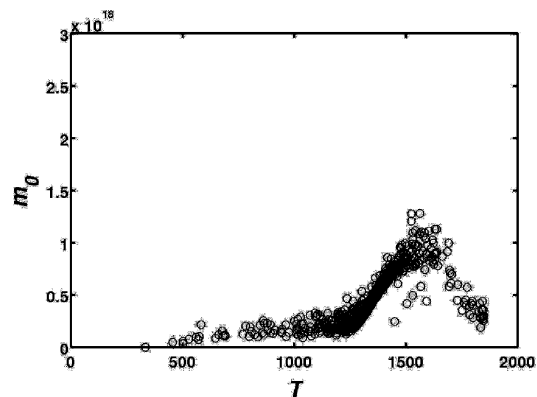
(a) Detailed flame, one-step nucleation



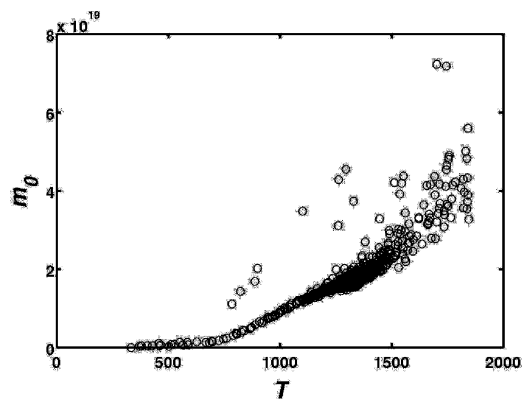
(b) Detailed flame, detailed nucleation



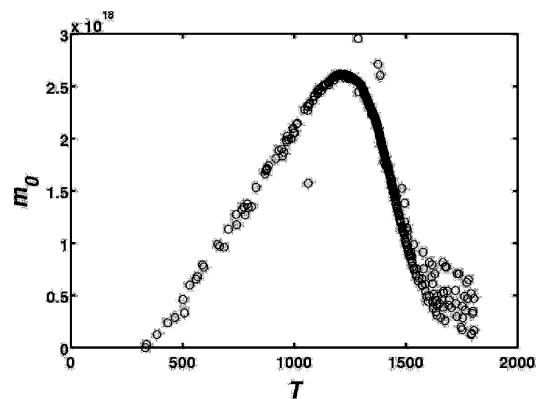
(c) Flamelet, one-step nucleation



(d) Flamelet, detailed nucleation



(e) All flamelet, one-step nucleation



(f) All flamelet, detailed nucleation

**Figure 5.** Scatter plots of number density ( $m_0$ ) versus temperature ( $T$ ) in PaSR.

The high air flow rates used in the experiments lead to immediate combustion and consumption of the precursor at the entrance of the jet. This leads to the production of nuclei immediately upstream of the jet. Since the objective of this paper is to examine the effect of the chemical mechanisms on nucleation, the residence time of the PaSR was chosen to predict the nucleation of particles in the upstream regions of the jet. Shorter residence times would ensure that nucleation dominates and the effect of using different mechanisms on the particle

inception process can be studied. The scalar dissipation was fixed at  $80.0 \text{ s}^{-1}$  for the PaSR simulation. This high value is intended to model the high shear region immediately downstream of the nozzle, where most of the nucleation occurs.

The plots shown in Figure 3a for both the detailed flame, one-step nucleation and the detailed flame, detailed nucleation reach the same temperature distribution at steady state. This tells us that the Ti-oxidation chemistry has no effect on the flame temperature for either the one-step or detailed nucleation. The

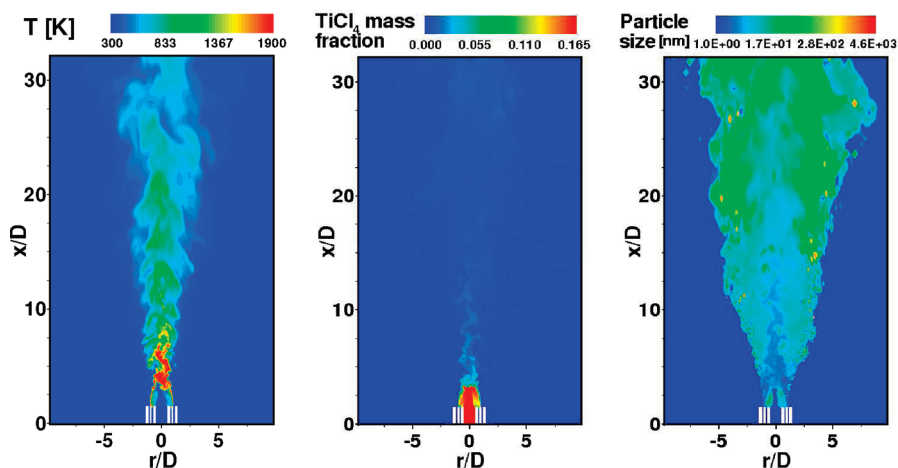


**Figure 6.** Temperature (left), precursor mass fraction (middle), and average particle size (right) obtained from LES.

predictions of temperature for all the cases involving flamelets are dependent on the mixture fraction and mixture-fraction dissipation rate. Because the same mixing time and the mixture-fraction dissipation rate are used for all the cases involving flamelets, the temperature evolution and the steady-state temperature are the same for all cases involving flamelets (see Figure 3b).

The one-step nucleation produces more nuclei ( $\langle m_0 \rangle = 7.26 \times 10^{18} \text{ m}^{-3}$ ) than detailed chemistry ( $\langle m_0 \rangle = 1.06 \times 10^{18} \text{ m}^{-3}$ ). This is expected, because the nuclei size for one-step chemistry is five times smaller than for detailed chemistry, so it produces  $\sim 5$  times more nuclei than the detailed mechanism. Because of the high air flow rates, most of the precursor is consumed on the lean side of the flame (here,  $\xi_{\text{air}} = 0$  and  $\xi_{\text{fuel}} = 1$ ). Therefore, we see that most of the nucleation happens near the mean mixture fraction at steady state ( $\xi = 0.1$ ) for all the models (see Figure 4). Similar to the PFR, the nucleation as predicted by the one-step mechanism occurs on the lean side of the flame ( $\xi < 0.1$ ). In contrast, for the detailed mechanism, nucleation occurs both on the lean side ( $\xi < 0.1$ ) and on the rich side ( $\xi > 0.1$ ) of the flame. We also see from these figures that the flamelet assumption can be used to represent the chemistry with reasonable accuracy (see Figures 4b and 4f); however, it does tend to overpredict the nucleation rate on the lean side of the flame (compare Figures 5b and 5f).

Because the particles are formed immediately upstream of the jet in the PaSR, the mean particle sizes predicted by all mechanisms are on the order of 10 nm (see Table 3). Both the back mixing in the PaSR and the high air flow rates ensure that the particles are distributed very close to the mean mixture fraction. The PaSR simulations examine the region very close to the jet exit. Thus, we observe that the particles have just started aggregating after nucleation in the PaSR, but the aggregation event has not started to dominate nucleation, which would result in larger particles. These particle sizes are also consistent with the results from LES discussed below.

The effect of temperature on the chemical mechanisms is depicted by Figure 5. The one-step mechanism, as in the PFR, produces a large number of particles immediately at the nozzle. As in the PFR, it was observed that, for the one-step nucleation, higher temperatures lead to higher number densities (see Figures 5a, 5c, and 5e). However, for the detailed mechanism, it is observed that the nucleation starts as the temperature approaches  $T = 1500 \text{ K}$ , but at  $T > 1800 \text{ K}$ , there is very little nucleation. This suggests, as we found in the PFR, that the particles undergo nucleation on both sides of the flame, as they cross from the

rich side to the lean side, because of mixing. The same trends are observed in the detailed flame, detailed nucleation and the flamelet, detailed nucleation cases (see Figures 3b and 3d). Thus, both the highly idealized case of a PFR (with no back mixing) and the more realistic case of a PaSR (with back mixing) show us that the choice of the nucleation chemistry model will be very important in predicting product properties (e.g., the extent of sintering).

**LES Results.** Figure 6 shows the instantaneous temperature and diameter obtained from the LES computations. The fuel and precursor enter the flow domain through the central jet. Since the coflow velocity is higher than the central jet velocity, a high-temperature zone is formed near the centerline very close to the jet exit. Further downstream, the lean fuel–air mixture leads to lower temperatures. The instantaneous precursor mass fraction contours show that at  $x/D \approx 4$ , the precursor is almost fully oxidized. The length-scale plot shows that the large number density near the primary oxidation zone leads to intense aggregation. The PSD can be analyzed by considering the evolution of the weights and abscissas. Figure 7 shows the time-averaged weights and abscissas at two different axial locations along the centerline. Both locations ( $x/D = 10$  and  $x/D = 30$ ) are downstream of the peak temperature zone seen in the instantaneous temperature plot (see Figure 6). It can be seen that all the peaks correspond to abscissas that are much larger than the nucleated particle size. However, the smallest abscissa is also associated with the largest weight, indicating that the true PSD is peaked at this size but has a long tail on the larger-diameter side. Note that the weights and abscissas do not change significantly between the two locations considered. This seems to indicate that both nucleation and aggregation are localized near the high-temperature zone. Beyond this region, most of the precursor has been oxidized leading to very limited nucleation. Aggregation rates (eq 9) increase quadratically with number density and linearly with temperature. Beyond the high-temperature zone at  $x/D \approx 5$ , both the number density and the temperature decrease rapidly. Consequently, the changes in the PSD are minimal.

## Conclusions

The effect of the chemical mechanism on the nucleation of titanium dioxide ( $\text{TiO}_2$ ) was studied for three flow models to take into account the turbulent flames in which these nanoparticles are produced. Three different mechanisms—one-step, detailed, and flamelet—were used to simulate the nanoparticle

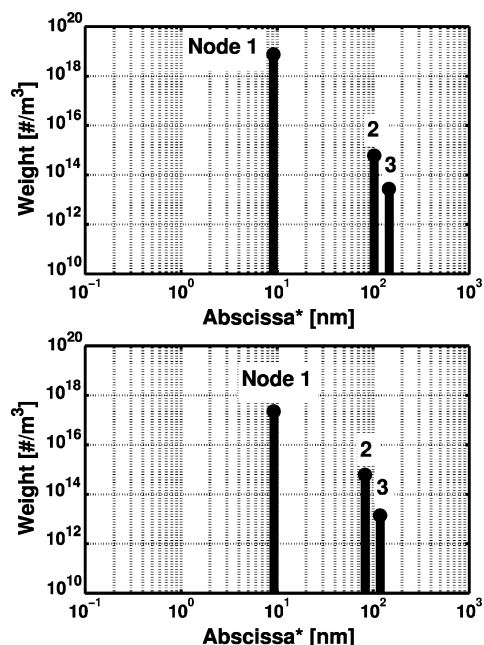


**Figure 7.** QMOM-based PSD at two downstream locations:  $x/D = 10$  (top) and  $x/D = 30$  (bottom). Length-based abscissas are computed based on eq 25.

nucleation process in an experimental setup.<sup>16</sup> A combination of one-step/detailed and flamelet table was also used to predict nanoparticle nucleation.

The experimental conditions result in most of the nucleation taking place immediately downstream of the nozzle. The results from the plug-flow reactor (PFR) show that, for one-step nucleation, the bulk of the nuclei are formed upstream of the flame surface and subsequently pass through the high-temperature region of the flame. In contrast, with the detailed nucleation model the bulk of the nuclei are formed downstream of the flame surface. These results suggest that the one-step nucleation model should predict very different high-temperature sintering behavior, compared to the detailed nucleation model.

The results from partially stirred tank reactor (PaSR) simulations show that vigorous back mixing within the turbulent flow results in more uniform particle properties, but the differences between the one-step and detailed nucleation models are still evident. The nucleation rate increases with temperature in the one-step nucleation and most of the nucleation happens on the lean side of the flame. In contrast, for the detailed mechanism nucleation happens in the range of 1500–1800 K, and thus occurs both on the lean side and the rich side of the flame. The large-eddy simulation (LES) results show particle formation with the one-step mechanism occurs very close to the flame surface (in agreement with the PFR and PaSR), and hence we would expect the detailed nucleation model to predict different aggregation and sintering characteristics when applied with LES.

For future work, we plan extend our LES study to different flow configurations using the detailed nucleation model. In addition, we plan to add a model for high-temperature sintering, to capture the effect of the location of primary nucleation (i.e., upstream of or downstream from the flame surface).

## Acknowledgment

The authors thank Prof. Sotiris Pratsinis (ETH Zürich) for valuable discussions and for providing the experimental details. This work was supported by NSF (through Grant No. CBET-

0730369). The authors also thank the Texas Advanced Computing Center for generous allocation of computing time.

## Literature Cited

- (1) Bankmann, M.; Brand, R.; Engler, B.; Ohmer, J. Forming of high surface area  $\text{TiO}_2$  to catalyst supports. *Catal. Today* **1992**, *14*, 225–242.
- (2) Wang, H.; Wu, Z.; Zhao, W.; Guan, B. Photocatalytic oxidation of nitrogen oxides using  $\text{TiO}_2$  loading on woven glass fabric. *Chemosphere* **2007**, *66*, 185–190.
- (3) Gonzalez, R.; Musick, C.; Tilton, J. Process for controlling agglomeration in the manufacture of  $\text{TiO}_2$ , U.S. Patent 5,508,015, April 16, 1996.
- (4) Deberry, J.; Robinson, M.; Pomponi, M.; Beach, A.; Xiong, Y.; Akhtar, K. Controlled vapor phase oxidation of titanium tetrachloride to manufacture titanium dioxide, U.S. Patent 6,387,347, May 14, 2002.
- (5) West, R. H.; Celnik, M. S.; Inderwildi, O. R.; Kraft, M.; Beran, G. J. O.; Green, W. H. Toward a comprehensive model of the synthesis of  $\text{TiO}_2$  particles from  $\text{TiCl}_4$ . *Ind. Eng. Chem. Res.* **2007**, *46*, 6147–6156.
- (6) Pratsinis, S. E.; Spicer, P. T. Competition between gas phase and surface oxidation of  $\text{TiCl}_4$  during synthesis of  $\text{TiO}_2$ . *Chem. Eng. Sci.* **1998**, *53*, 1861–1868.
- (7) Spicer, P. T.; Chaoul, O.; Tsantilis, S.; Pratsinis, S. E. Titania formation by  $\text{TiCl}_4$  gas phase oxidation, surface growth and coagulation. *J. Aerosol Sci.* **2002**, *33*, 17–34.
- (8) Heine, M. C.; Mädler, L.; Jossen, R.; Pratsinis, S. E. Direct measurement of entrainment during nanoparticle synthesis in spray flames. *Combust. Flame* **2006**, *144*, 809–820.
- (9) Pitsch, H. Large-eddy simulation of turbulent combustion. *Annu. Rev. Fluid Mech.* **2006**, *38*, 453–482.
- (10) Kempf, A.; Lindstedt, R. P.; Janicka, J. Large-Eddy Simulation of Bluff-Body Stabilized Nonpremixed Flame. *Combust. Flame* **2006**, *144*, 170–189.
- (11) Raman, V.; Pitsch, H. Large-eddy simulation of a bluff-body-stabilized non-premixed flame using a recursive filter-refinement procedure. *Combust. Flame* **2005**, *12*, 329–347.
- (12) Raman, V.; Pitsch, H. A consistent LES/filtered-density function formulation for the simulation of turbulent flames with detailed chemistry. *Proc. Combust. Inst.* **2006**, *31*, 1711–1719.
- (13) Raman, V.; Pitsch, H.; Fox, R. O. Eulerian transported probability density function sub-filter model for large-eddy simulation of turbulent combustion. *Combust. Theor. Model* **2006**, *10*, 439–458.
- (14) Menon, S.; Patel, N. Subgrid modeling for simulation of spray combustion in large-scale combustors. *AIAA J.* **2006**, *44*, 709–723.
- (15) Peters, N. *Turbulent Combustion*; Cambridge University Press: Cambridge, U.K., 2000.
- (16) Pratsinis, S. E.; Zhu, W.; Vemury, S. The role of gas mixing in flame synthesis of titania powders. *Powder Technol.* **1996**, *86*, 87–93.
- (17) Marchisio, D. L.; Vigil, R. D.; Fox, R. O. Quadrature method of moments for aggregation-breakage processes. *J. Colloid Interface Sci.* **2003**, *258*, 322–334.
- (18) Karlemo, B.; Koukkari, P.; Paloniemi, J. Formation of gaseous intermediates in titanium(IV) chloride oxidation. *Plasma Chem. Plasma Process.* **1996**, *16*, 59–77.
- (19) Pratsinis, S.; Bai, H.; Biswas, P.; Frenklach, M.; Mastrangelo, S. Kinetics of titanium(IV) chloride oxidation. *J. Am. Ceram. Soc.* **1990**, *73*, 2158–2162.
- (20) Tsantilis, S.; Pratsinis, S. E. Narrowing the size distribution of aerosol-made titania by surface growth and coagulation. *J. Aerosol Sci.* **2004**, *35*, 405–420.
- (21) Morgan, N. M.; Wells, C. G.; Goodson, M. J.; Kraft, M.; Wagner, W. A new numerical approach for the simulation of the growth of inorganic nanoparticles. *J. Comput. Phys.* **2006**, *211*, 638–658.
- (22) Heine, M. C.; Pratsinis, S. E. Agglomerate  $\text{TiO}_2$  aerosol dynamics at high concentrations. *Part. Part. Syst. Charact.* **2007**, *24*, 56–65.
- (23) Heine, M. C.; Pratsinis, S. E. Polydispersity of primary particles in agglomerates made by coagulation and sintering. *J. Aerosol Sci.* **2007**, *38*, 17–38.
- (24) Ghoshtagore, R. N. Mechanism of heterogeneous deposition of thin film rutile. *J. Electrochem. Soc.: Solid State Sci.* **1970**, *117*, 529–534.
- (25) West, R. H.; Shirley, R. A.; Kraft, M.; Goldsmith, C. F.; Green, W. H. A detailed kinetic model for combustion synthesis of titania from  $\text{TiCl}_4$ . *Combust. Flame* **2009**, *156*, 1764–1770.
- (26) West, R. H.; Beran, G. J. O.; Green, W. H.; Kraft, M. First-principles thermochemistry for the production of  $\text{TiO}_2$  from  $\text{TiCl}_4$ . *J. Phys. Chem. A* **2007**, *111*, 3560–3565.

- (27) Bowman, C.; Hanson, R.; Davidson, D.; Gardiner, W., Jr.; Lissianski, V.; Smith, G.; Golden, D.; Frenklach, M.; Goldenberg, M. GRI-Mech 2.11. Available via the Internet at [http://www.me.berkeley.edu/gri\\_mech/](http://www.me.berkeley.edu/gri_mech/).
- (28) *Sixth International Workshop on Measurement and Computation of Turbulent Non-premixed Flames*, Sapporo, Japan, 2002.
- (29) Pitsch, H. A C++ Computer Program for 0-D and 1-D Laminar Flame Calculations; Technical Report, RWTH Aachen, Aachen, Germany, 1998.
- (30) Fox, R. O. *Computational Models for Turbulent Reacting Flows*; Cambridge Series in Chemical Engineering; Cambridge University Press: Cambridge, U.K., 2003.
- (31) Xiong, Y.; Pratsinis, S. E. Formation of agglomerate particles by coagulation and sintering—Part I: A two-dimensional solution of the population balance equation. *J. Aerosol Sci.* **1993**, *3*, 283–300.
- (32) Marchisio, D. L.; Vigil, R. D.; Fox, R. O. Implementation of the quadrature method of moments in CFD codes for aggregation-breakage problems. *Chem. Eng. Sci.* **2003**, *58*, 3337–3351.
- (33) Mingzhou, Y.; Jianzhong, L.; Hongbing, X. Quadrature method of moments for nanoparticle coagulation and diffusion in the planar impinging jet flow. *Chin. J. Chem. Eng.* **2007**, *15*, 828–836.
- (34) McGraw, R. Description of aerosol dynamics by the quadrature method of moments. *Aerosol Sci. Technol.* **1997**, *27*, 255–265.
- (35) Cheng, J. C.; Fox, R. O. Kinetic modeling of nanoprecipitation using CFD coupled with a population balance. Submitted to *Ind. Eng. Chem. Res.*, **2010**.
- (36) Friedlander, S. K. *Smoke, dust, and haze—Fundamentals of aerosol dynamics*; Oxford University Press: Oxford, U.K., 2000.
- (37) Pope, S. B. *Turbulent Flows*; Cambridge University Press: Cambridge, U.K., 2000.
- (38) Sabel'Nikov, V.; Silva, L. D. Partially stirred reactor: Study of the sensitivity of the Monte-Carlo simulation to the number of stochastic particles with the use of a semi-analytic, steady-state, solution to the PDF equation. *Combust. Flame* **2002**, *129*, 164–178.
- (39) Ren, Z.; Pope, S. B. An investigation of the performance of turbulent mixing models. *Combust. Flame* **2004**, *136*, 208–216.
- (40) Smagorinsky, J. General circulation experiments with the primitive equations: I. The basic equations. *Mon. Weather Rev.* **1963**, *91*, 99–164.
- (41) Germano, M. Turbulence: The filtering approach. *J. Fluid Mech.* **1991**, *286*, 229–255.
- (42) Moin, P.; Squires, K.; Cabot, W.; Lee, S. A dynamic subgrid-scale model for compressible turbulence and scalar transport. *Phys. Fluids A* **1991**, *3*, 2746–2757.
- (43) Ghosal, S.; Lund, T. S.; Moin, P.; Akselvoll, K. A dynamic localization model for large-eddy simulation of turbulent flows. *J. Fluid Mech.* **1995**, *286*, 229–255.
- (44) Wall, C.; Boersma, B.; Moin, P. An evaluation of the assumed beta probability density function sub-grid scale model for large eddy simulation of non-premixed turbulent combustion with heat release. *Phys. Fluids* **2000**, *7*, 2522–2529.
- (45) Pierce, C. D.; Moin, P. A dynamic model for subgrid-scale variance and dissipation rate of a conserved scalar. *Phys. Fluids* **1998**, *10*, 3041–3044.
- (46) Akselvoll, K.; Moin, P. Large eddy simulation of turbulent confined coannular jets. *J. Fluid Mech.* **1996**, *315*, 387–411.
- (47) Pierce, C. D. Ph.D. thesis, Stanford University, Palo Alto, CA, 2001.
- (48) Desjardins, O.; Blanquart, G.; Balarac, G.; Pitsch, H. High order conservative finite difference scheme for variable density low Mach number turbulent flows. *J. Comput. Phys.* **2008**, *227*, 7125–7159.
- (49) Leonard, B. P. A stable and accurate convective modelling procedure based on quadratic upstream interpolation. *Comput. Methods Appl. Mech. Eng.* **1979**, *19*, 59–98.
- (50) Herrmann, M.; Blanquart, G.; Raman, V. A bounded QUICK scheme for preserving scalar bounds in large-eddy simulations. *AIAA J.* **2006**, *44*, 2879–2886.

Received for review March 9, 2010

Revised manuscript received May 18, 2010

Accepted May 19, 2010

IE100560H